Near-field correlations in the two-photon field

Lorenzo Pires, H. di; Exter, M.P. van

Near-field correlations in the two-photon field

H. Di Lorenzo Pires* and M. P. van Exter†
Huygens Laboratory, Leiden University, P.O. Box 9504, 2300 RA Leiden, The Netherlands
(Received 8 July 2009; published 13 November 2009)

In experiments with spontaneous parametric down conversion the near-field plane is usually defined as the output facet of the generating crystal. Experimentally, however, the spatial correlations are accessed via an imaging system and observed in a region around the image of the output facet. We show that the imaged two-photon field has a very rich transverse and longitudinal structure, which is determined by the phase-matching conditions. We observe many intriguing three-dimensional structures that demonstrate the presence of spatial antibunching, an extreme localization of twin photons, and spatial correlations that resemble Bessel beams in propagation. We link these observations with previous results in second harmonic generation and predict the presence of fourth-order phase singularities. Both experiments and theory are presented, yielding further insight into the nature of the two-photon field.

DOI: 10.1103/PhysRevA.80.053820 PACS number(s): 42.65.Lm, 03.67.Mn, 42.50.Dv

I. INTRODUCTION

Observations of multifold photon count statistics have played a major role in both classical and quantum optics since the seminal paper of Hanbury Brown and Twiss [1]. A prominent example of a field that displays intriguing higher-order correlations is the two-photon field generated by spontaneous parametric down conversion (SPDC) [2,3]. In this process a laser beam pumps a dielectric nonlinear crystal, generating highly correlated pairs of down-converted photons. These so-called "twin photons" or "biphotons" have been employed in several landmark experiments on fundamental concepts of quantum mechanics, such as violation of Bell's inequalities [4,5], quantum teleportation [6], quantum criptography [7], and a realization of the EPR paradox using momentum and position entangled photons [8]. SPDC light still stands out as the most versatile sources of entangled photon pairs.

Having a wide range of applications, full knowledge of the spatial properties of the two-photon field generated by SPDC is highly desirable. The quantum aspects of the spatial correlations are revealed not in the lowest-order correlation function, associated with the "one-photon" spatial coherence, but in the next higher order, which can be probed in the laboratory by performing two-photon coincidence measurements. These nonclassical correlations are a signature of the spatial (mode) entanglement, which makes SPDC interesting for the field of quantum information.

The complete wave-function of the two-photon field generated by SPDC is well known from theory [8–11]. It contains two essential ingredients, being the shape of the pump beam and the phase-matching conditions associated with the crystal geometry. The *angular* representation of this two-photon field has been studied extensively. Its contains a substructure that includes the full spatial information of the pump beam [12] and that shows up only in the fourth-order field correlations, but not in the second-order ones. As such, these angular correlations have formed the basis of many quantum experiments with entangled photon pairs. On the other hand, the *spatial* representation of the generated two-photon field has been hardly studied and many intriguing aspects of this field have gone unnoticed up to now. These spatial aspects, which we will denote as "near-field correlations" or "fine structure" of the two-photon field, form the heart of this paper. They are associated with the phase matching of the SPDC process [9,13,14]. Their theoretical description requires one to go beyond the Gaussian approximation of phase matching [15], or the delta-type approximation applicable to thin crystals, but use the proper phase-matching condition instead [8–11].

Experimentally, the near-field correlations are measured by imaging the output facet of the generating crystal on the detection plane. For instance, a single plane measurement at perfect phase matching has been used in a realization of the Einstein-Podolsky-Rosen paradox [8]. This measurement was then interpreted as an image of the relative birthplace of down-converted photons. One must realize, however, that SPDC is a coherent process in which light generated at all transverse planes inside the crystal contributes to the measured field in the image plane. In other words, an image of the output facet of the crystal does not simply provide information about the relative birthplace of the photon pairs, but is a consequence of a fourth-order interference effect. As we will show, the symmetry of the process is such that an "image" of the input facet of the crystal provides exactly the same transverse correlations as one from the output facet. However, strong differences arise if one images the center of the crystal. Contrary to what is usually believed, the transverse and longitudinal correlations in the vicinity of the image plane are nontrivial and reveal a very rich structure.

In this paper we will show experimentally how the finite thickness of the crystal results in a rich set of spatial correlations in the image plane of the crystal. The complete spatial dependence, both in transverse and longitudinal coordinates, is presented. Operation under phase mismatch leads to many intriguing effects and will be extensively discussed. A few results were already introduced by us in Ref. [16]. Here we will present the theoretical framework, new experimental results, and discussions about many physical consequences of

*pires@molphys.leidenuniv.nl
†mvexter@molphys.leidenuniv.nl

the near-field strucutre. Among them, the presence of spatial antibunching, the observation of extreme localization of twin photons, a link with previous results in second harmonic generation, the observation of correlations that resemble Bessel beams in propagation, and the prediction of fourth-order phase singularities. Section II contains the theoretical basis of our work, Sec. III lists the experimental results, and Sec. IV the conclusions and discussion of future perspectives.

II. THEORY

Spatially entangled photon pairs can be generated by the nonlinear optical process of spontaneous parametric down conversion, where a single pump photon "splits" into two lower-energy photons, which are traditionally called signal and idler. We can think of the crystal as being a thick and extended source of very many elementary "radiators." The SPDC light behaves as a low-coherence light source as long as the emitted photons are detected individually [17–19]. Most interesting effects are only revealed when one looks at the correlations between the positions of the detected photons. From the quantum theory of optical coherence the probability of detecting twofold delayed coincidences, for light in a arbitrary quantum state Ψ, is given by the fourth-order correlation function

$$\Gamma^{(4)}(\boldsymbol{r}_1,t_1;\boldsymbol{r}_2,t_2)=\langle\Psi|\hat{E}^-(\boldsymbol{r}_1,t_1)\hat{E}^-(\boldsymbol{r}_2,t_2)\hat{E}^+(\boldsymbol{r}_2,t_2)\hat{E}^+(\boldsymbol{r}_1,t_1)|\Psi\rangle, \tag{1}$$

where $\boldsymbol{r}_i$ and t_i are the position and detection time of a photon in detector $i=1,2$. If Ψ represents light in a two-photon state, as it happens in SPDC, the correlation function can be further decomposed as

$$\Gamma^{(4)}(\boldsymbol{r}_1,t_1;\boldsymbol{r}_2,t_2)=|\psi(\boldsymbol{r}_1,t_1;\boldsymbol{r}_2,t_2)|^2, \tag{2}$$

where the two-photon probability amplitude

$$\psi(\boldsymbol{r}_1,t_1;\boldsymbol{r}_2,t_2)=\langle 0|\hat{E}^+(\boldsymbol{r}_1,t_1)\hat{E}^+(\boldsymbol{r}_2,t_2)|\Psi\rangle \tag{3}$$

is sometimes referred to as the wave function of the state. From now on we will restrict ourselves to coincidence detection in a single z plane at $t_1\approx t_2$ and denote $\psi(\boldsymbol{r}_1,t_1;\boldsymbol{r}_2,t_2)=A(\boldsymbol{\rho}_1,\boldsymbol{\rho}_2;z)$ as the SPDC probability amplitude. Throughout the paper we use a cylindrical coordinate system with the z axis coinciding with the pump beam axis and with $\boldsymbol{r}=(\boldsymbol{\rho},z)$ being the position vector, with transverse $\boldsymbol{\rho}$ and longitudinal z components. A crucial element in our discussion is the assumption that the pump laser is relatively wide as compared to the near-field correlations under study. The two-photon field will then depend dominantly on the difference coordinate $\boldsymbol{\rho}_-=\boldsymbol{\rho}_1-\boldsymbol{\rho}_2$ in the near field, making $A(\boldsymbol{\rho}_1,\boldsymbol{\rho}_2;z)\approx V(\boldsymbol{\rho}_1-\boldsymbol{\rho}_2;z)$ (see Secs. II A and II B for details). The thin-crystal limit consists on approximating $V(\boldsymbol{\rho}_-;z)$ by a δ function. This article discusses specifically how the fine-structure function $V(\boldsymbol{\rho}_-;z)$ looks like beyond this δ limit.

The near field is usually defined in optics as the field distribution at the source. For a thick (=longitudinally extended) source this concept is ill defined and, as we will show later, the results depend strongly on which z plane of our thick source is imaged. Whatever the imaging geometry, photon pairs emitted from all planes within the crystal will always contribute coherently to the two-photon field in the image plane. Throughout the article we will use the term "near field" to denote the field in a certain z plane around the image plane of the center of the generating crystal, which we define as $z=0$. In contrast, the far field is defined as the amplitude distribution in a very distant transverse z plane. The transition from the near field to the far field can be done by either propagating the generated field or by performing a (fractional) Fourier transformation [20–23].

In the next subsections we will present two different models to calculate the amplitude function $V(\boldsymbol{\rho}_-;z)$. The first approach (Sec. II A) starts from the angular spectrum of the generated field, which is then Fourier transformed to the spatial domain. The detection process is included afterwards. The second approach (Sec. II B) is formulated directly in spatial coordinates and treats the generation and detection processes on equal footing. While the first approach can be easily compared to results already presented in the literature, the second approach is less common and permits more insight into the nature of the two-photon field. Naturally, both approaches lead to the same predictions.

The main differences between our approach and other equations presented in the literature [24–26] are the following. First, we treat the transverse plane in two dimensions. Assuming a one-dimensional system does lead to loss of generality in our case. Second, we use a generalized "Klyshko picture" in order to account for the non-thin-crystal assumption. And third, the detection geometry must be included in the description in order to obtain the correct working equations.

A. Analysis based on the angular spectrum

The momentum representation of the two-photon field generated by SPDC is [2,12],

$$\tilde{A}(\boldsymbol{q}_s,\boldsymbol{q}_i)=\tilde{E}(\boldsymbol{q}_s+\boldsymbol{q}_i)\mathrm{sinc}\left(\frac{1}{2}\Delta k_z L\right), \tag{4}$$

where $\tilde{E}(\boldsymbol{q})$ is the angular spectrum of the pump beam and $\mathrm{sinc}(\frac{1}{2}\Delta k_z L)$ is the phase-matching function, with $\mathrm{sinc}(x)=\sin(x)/x$, and crystal thickness L. Phase matching plays a crucial role in all nonlinear optical process. The conversion efficiency is maximum if the interacting optical waves retain a fixed phase relation over the full length of the nonlinear crystal. This is expressed mathematically by the dependence of the "sinc" function on the longitudinal wave-vector mismatch $\Delta k_z=k_{p,z}-k_{s,z}-k_{i,z}$, where the indices refers to the pump (p), signal (s), and idler (i) photons, respectively.

We will concentrate now on our particular case of SPDC emission. We consider noncritical type I phase matching, where all polarizations are equal and all beams propagate close to a principal crystal axis in a periodically poled crystal. These crystals offer the advantage of having a high conversion efficiency, when compared to bulk crystals. Addi-

tionally, the photon pairs do not suffer Poyinting vector walk off. With regard to the generated wave function, i.e., the spatial correlations, SPDC light produced in a periodically polled crystal behave exactly the same as in a bulk crystal [27,28]. A second-order Taylor expansion of the quasi-wave-vector mismatch Δk_z in the considered geometry yields [29]

$$\tfrac{1}{2}\Delta k_z L \approx \frac{L}{8nk_0}\left[|\boldsymbol{q}_s-\boldsymbol{q}_i|^2+\left(\frac{n_p-n}{n_p}\right)|\boldsymbol{q}_s+\boldsymbol{q}_i|^2\right]+\varphi(T,\Omega), \tag{5}$$

where $k_0=2\pi/\lambda_0$ is the vacuum wave vector of the generated light, n_p and n are the refractive indices at the pump and generated wavelength, respectively, and $\boldsymbol{q}_{s,i}$ are the transverse components of the signal and idler wave vectors $\boldsymbol{k}_{s,i}$; the angular dependence of n_p and n has been neglected. In our further analysis we will neglect the minor dependence of the phase mismatch on the sum momentum because (i) typically the ratio $(n_p-n)/n_p \ll 1$, being 0.058 for our periodically poled KTP, and (ii) the spread in the sum momentum $\boldsymbol{q}_s+\boldsymbol{q}_i$, as set by the pump divergence, is generally much smaller than the spread in the difference momentum $\boldsymbol{q}_s-\boldsymbol{q}_i$, anyhow.

Under the conditions stated above, the angular spectrum of the generated two-photon field thus factorizes in the special form [11,12]

$$\tilde{A}(\boldsymbol{q}_s,\boldsymbol{q}_i)=\tilde{E}_p(\boldsymbol{q}_s+\boldsymbol{q}_i)\tilde{V}(\boldsymbol{q}_s-\boldsymbol{q}_i), \tag{6}$$

where the phase-matching function $\tilde{V}(\boldsymbol{q}_s-\boldsymbol{q}_i)=\mathrm{sinc}(\frac{1}{2}\Delta k_z L)$ depends only on the difference momentum. This function also contains the collinear phase mismatch φ as an adjustable parameter that depends on the crystal temperature T and a possible frequency detuning $\Omega \ll \omega_0$ from frequency degeneracy as [27]

$$\varphi(T,\Omega)=\alpha(T-T_0)-\beta\Omega^2. \tag{7}$$

The two-photon field in real-space coordinates $A(\boldsymbol{\rho}_s,\boldsymbol{\rho}_i;z)$ can be obtained from a Fourier transformation that links the transverse momentum $\boldsymbol{q}$ with the transverse position $\boldsymbol{\rho}$ for both signal and idler photons. Based on Eq. (6), it is straightforward to show that the spatial representation of the two-photon field can also be factorized as

$$A(\boldsymbol{\rho}_s,\boldsymbol{\rho}_i;z)=E_p(\boldsymbol{\rho}_+;z)V(\boldsymbol{\rho}_-;z). \tag{8}$$

The factor $E_p(\boldsymbol{\rho}_+;z)$ quantifies the well-known observation that the two-photon field retains a "copy of the pump profile" [12] in its dependence on the average coordinate $\boldsymbol{\rho}_+\equiv\frac{1}{2}(\boldsymbol{\rho}_s+\boldsymbol{\rho}_i)$. The factor $V(\boldsymbol{\rho}_-;z)$ quantifies the fine structure in the two-photon field via its dependence on the difference coordinate $\boldsymbol{\rho}_-\equiv(\boldsymbol{\rho}_s-\boldsymbol{\rho}_i)$. Note that Eq. (8) describes the total two-photon field as observed around an image plane of the generating crystal. In the $z=0$ image plane, associated with the center of the crystal, Eq. (6) contains no extra phase factors. For points in the vicinity of this plane (at $z\neq 0$) the angular spectrum must be multiplied by the free space propagator $\exp[-i|\boldsymbol{q}|^2 z/(2k)]$ for both the signal and idler photons.

Experimentally, the fine structure described by the function $V(\boldsymbol{\rho}_-,z)$ can be most easily observed if it exists on a scale much smaller than the pump profile, making $A(\boldsymbol{\rho}_s,\boldsymbol{\rho}_i;z)=E_p(\boldsymbol{\rho}_+;z)V(\boldsymbol{\rho}_-;z)\approx V(\boldsymbol{\rho}_-;z)$. This condition is satisfied in the near field if the pump laser is sufficiently well collimated, i.e., if the Rayleigh range of the pump laser is much larger than the thickness of the crystal. Based on Eqs. (4) and (5) we write $\tilde{V}(\boldsymbol{q}_s-\boldsymbol{q}_i)=\mathrm{sinc}[(L/8nk_0)|\boldsymbol{q}_s-\boldsymbol{q}_i|^2+\varphi]$, which after Fourier transformation yields

$$V(\boldsymbol{\rho}_-;z)\propto\int_{-\infty}^{+\infty}d\boldsymbol{q}\ \ \mathrm{sinc}\left(\frac{L|\boldsymbol{q}|^2}{2nk_0}+\varphi\right)\exp\left[-i\frac{|\boldsymbol{q}|^2}{k_0}z-i\boldsymbol{q}\cdot\boldsymbol{\rho}_-\right]. \tag{9}$$

We experimentally measure the fine structure in the generated two-photon field with two-photon counting modules that are coupled to moveable single-mode fibers. Mathematically, this detection geometry is described by a projection of the two-photon amplitude onto the mode profiles of the two detectors. This yields the projected amplitude

$$V_{\mathrm{proj}}(\boldsymbol{\rho}_s-\boldsymbol{\rho}_i;z)\propto\int_{-\infty}^{+\infty}\int d\boldsymbol{\rho}_s' d\boldsymbol{\rho}_i' V(\boldsymbol{\rho}_s'-\boldsymbol{\rho}_i';z)\phi_s^*(\boldsymbol{\rho}_s'-\boldsymbol{\rho}_s;z)\phi_i^*(\boldsymbol{\rho}_i'-\boldsymbol{\rho}_i;z), \tag{10}$$

where $\phi_j(\boldsymbol{\rho}_j;z)$ is the mode profile of either detector mode ($j=\{s,i\}$) and $\boldsymbol{\rho}_j$ is now the adjustable displacement of this detector. The integration over the transverse coordinates can be taken in any z plane because the propagation of the two-photon field is described by the product of the same single-mode propagators that determine the propagation of the detector modes. The coincidence count rate $R_{cc}\propto|V_{\mathrm{proj}}(\boldsymbol{\rho}_s-\boldsymbol{\rho}_i;z)|^2$. This function is rotationally symmetric, as it depends only on $|\boldsymbol{\rho}_s-\boldsymbol{\rho}_i|$, and possesses mirror symmetry with respect to the $z=0$ plane, since $V_{\mathrm{proj}}(\boldsymbol{\rho}_-;z)=V_{\mathrm{proj}}^*(\boldsymbol{\rho}_-;-z)$. Further simplifications of Eq. (10) will be provided in the Appendix A, which includes an analytical expression for the on-axis correlations at perfect phase matching ($\varphi=0$).

Although the above discussion started from noncritical type I phase-matching conditions, it also applies to general type I phase matching, where the beams are not necessarily aligned with the crystal axes, and even works partially for general type II phase matching. The argument goes as follows. For any type of phase matching, we can always rewrite the general Eq. (4) in the form

$$\tilde{A}(\boldsymbol{q}_s,\boldsymbol{q}_i)=\tilde{E}(\boldsymbol{q}_s+\boldsymbol{q}_i)\hat{V}(\boldsymbol{q}_s+\boldsymbol{q}_i,\boldsymbol{q}_s-\boldsymbol{q}_i), \tag{11}$$

where the new phase-matching function $\hat{V}$ now depends both on the sum and difference coordinate. As essential ingredient, we again assume that the pump profile is sufficiently wide in real space in order to make $\tilde{E}(\boldsymbol{q}_s+\boldsymbol{q}_i)$ compact enough in momentum space to dominate over a possible dependence of $\hat{V}$ on $\boldsymbol{q}_s+\boldsymbol{q}_i$. This allows us to approximate $\tilde{A}(\boldsymbol{q}_s,\boldsymbol{q}_i)\approx\hat{V}(\boldsymbol{0},\boldsymbol{q}_s-\boldsymbol{q}_i)\equiv\tilde{V}(\boldsymbol{q}_s-\boldsymbol{q}_i)$, although the precise expression for $\tilde{V}$ depends on the type of phase matching (see Appendix of Ref. [30]). For general type I phase matching we again obtain $\tilde{V}(\boldsymbol{q}_s-\boldsymbol{q}_i)=\mathrm{sinc}[(L/8nk_0)|\boldsymbol{q}_s-\boldsymbol{q}_i|^2+\varphi]$, but the assumption "sufficiently wide pump," now also requires that the pump beam is wider than the transverse walk off

between the pump beam and SPDC beams on top of the original requirement $z_n \gg L$. For type II SPDC, the walk off between the (orthogonally polarized) signal and idler photons introduces an extra linear form in the phase-matching function, which now becomes $\tilde{V}(\boldsymbol{q}_s - \boldsymbol{q}_i) = \mathrm{sinc}[(L/8nk_0)|\boldsymbol{q}_s - \boldsymbol{q}_i|^2 + \gamma(q_{s,y} - q_{i,y}) + \varphi]$. After Fourier transformation, the spatial correlation observable in the fine-structure function $V(\boldsymbol{\rho}_-; z)$ are found to have lost their rotation symmetry; the correlations in the x direction, i.e., orthogonal to the walk off direction, are as before but the correlations in the y direction are naturally stretched by the transverse walk off in that direction.

B. Analysis based on volume integral over detection modes

In this subsection we will present an alternative approach to calculate the projected field $A_{\mathrm{project}}(\boldsymbol{\rho}_s, \boldsymbol{\rho}_i; z)$ directly in real space, without the detour via its angular spectrum. This approach is based on a three-dimensional integration over the production sites of photon pairs within the generating crystal.

In SPDC, the probability amplitude for the pump photon to split into two lower-energy photons is proportional to the complex electric field at the generating site. As the photon pairs are always emitted "from the same point," one can write [31]

$$A_{source}(\boldsymbol{r}_s', \boldsymbol{r}_i') \propto E_p(\boldsymbol{r}_s')\,\delta(\boldsymbol{r}_s' - \boldsymbol{r}_i'), \tag{12}$$

where $E_p(\boldsymbol{r}_s')$ is the electric field profile of the pump beam. The probability amplitude of finding two photons at positions $\boldsymbol{r}_s$ and $\boldsymbol{r}_i$ outside the crystal is obtained by summation over all possible generating sites and propagation to the observation points. This leads to the following integral:

$$A_{gen}(\boldsymbol{\rho}_s, \boldsymbol{\rho}_i; z) = \int_{crystal} d\boldsymbol{\rho}'\, dz'\, E_p(\boldsymbol{\rho}', z') \times h(\boldsymbol{\rho}_s, z; \boldsymbol{\rho}', z') h(\boldsymbol{\rho}_i, z; \boldsymbol{\rho}', z'), \tag{13}$$

where $h(\boldsymbol{\rho}, z; \boldsymbol{\rho}', z')$ is the Green's function that describes the propagation of the field from the plane z to the plane z'. Equation (13) can be considered as a generalization of the result presented in Ref. [31], the major difference being the inclusion of the z integration to account for the finite crystal thickness. Since our crystal is a longitudinally extended source and the propagators $h(\boldsymbol{\rho}, z; \boldsymbol{\rho}', z')$ links the field between any two planes, Eq. (13) basically integrates the contributions of all different generating planes to the observation plane. This generalization is sufficient to explain *all* results presented in this paper.

In our experimental scheme the down-converted beams are detected by single-mode optical fibers. One can then use both propagators h to propagate the well-defined detection modes *back* to the crystal, instead of using the *forward* propagation of the generated two-photon field toward the detectors. We will denominate this point of view as the "double Klyshko picture," in analogy with the Klyshko picture of SPDC where only one beam is propagated backward from the detector to the generating crystal, where it is effectively "reflected" toward the other detector. The double Klyshko picture considerably simplifies the description since the Gaussian profiles of the detection modes can be easily propagated.

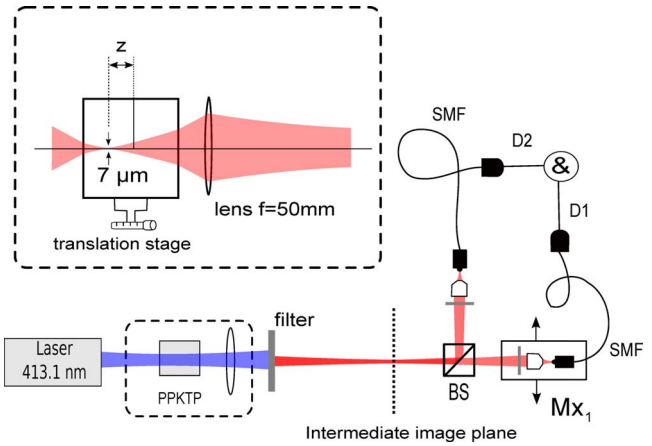

FIG. 1. (Color online) Experimental setup for observing the near-field correlations in the two-photon field. A PPKTP crystal is pumped by a laser beam operating at 413.1 nm, generating photon pairs by SPDC. A $f=50$ mm lens creates a 13× magnified image of the near field in a intermediate plane. The two-photon field is then separated at a beam splitter, projected onto two single-mode optical fibers by objective lenses, and detected by photon counters and coincidence electronics. Interference filters are used to block the pump wavelength after the crystal and to select photons close to frequency degeneracy in front of the detectors (spectral width 5 nm at 826 nm). The transverse correlations within the photon pairs are measured by moving detector 1 horizontally; the longitudinal correlations are obtained by adjusting the crystal z position with a translation stage. The inset shows how the detection modes would behave inside the crystal if back propagated through the imaging system. The detection waist of 7 μm was chosen to provide an optimal tradeoff between resolution and detection efficiency.

For a crystal of thickness L in the z direction and infinite width in the transverse directions we may thus write the projected two-photon field as

$$A_{\mathrm{proj}}(\boldsymbol{\rho}_s, \boldsymbol{\rho}_i; z) \propto \int_{-L/2}^{+L/2} dz' \int_{-\infty}^{+\infty} d\boldsymbol{\rho}'\, E_p(\boldsymbol{\rho}'; z') \times \phi_s^*(\boldsymbol{\rho}' - \boldsymbol{\rho}_s; z' - z)\, \phi_i^*(\boldsymbol{\rho}' - \boldsymbol{\rho}_i; z' - z), \tag{14}$$

where $\boldsymbol{\rho}_s$ and $\boldsymbol{\rho}_i$ again denote the transverse displacement of the detection modes. In the "double Klyshko picture" we can also consider z as the position of the detection modes foci *inside the crystal*, as shown in the inset of Fig. 1. The mode profile of each fundamental Gaussian detecting modes is

$$\phi(\boldsymbol{\rho}; z) \propto \frac{\exp(ikz)}{z - iz_n} \exp\left[i \frac{k|\boldsymbol{\rho}|^2}{2(z - iz_n)} \right] = \frac{\exp\{i[kz - \phi_{\mathrm{Gouy}}(z)]\}}{\sqrt{z^2 + z_n^2}} \exp\left[-\frac{|\boldsymbol{\rho}|^2}{w(z)^2} \right] \exp\left[i \frac{k|\boldsymbol{\rho}|^2}{2R(z)} \right], \tag{15}$$

where $z_n=\frac{1}{2}nk_0w_d^2$ is the Rayleigh range, $\phi_{\text{Gouy}}(z)=\arctan(z/z_n)$ is the Gouy phase, $w(z)=w_d\sqrt{1+z^2/z_n^2}$ is the beam diameter, and $R(z)=z+z_n^2/z$ is the radius of curvature of the detection mode. Upon entering a dielectric medium, the Gaussian detection mode retains its waist w_d but is stretched in the longitudinal direction; this effect has been accounted for by introducing z_n and $k=nk_0$.

Finally, we substitute the mode profiles of Eq. (15) in Eq. (14) and consider a very wide pump beam. A Gaussian integration over the transverse coordinates allows us to express the projected field in terms of a single integral over the thickness of the crystal

$$V_{\text{proj}}(\boldsymbol{\rho}_s-\boldsymbol{\rho}_i;z)\propto\int_{-L/2-nz}^{+L/2-nz}dz'\frac{\exp(-i\Delta k_z^0z')}{z'-iz_n}\times\exp\left(\frac{ik}{z'-iz_n}\frac{|\boldsymbol{\rho}_s-\boldsymbol{\rho}_i|^2}{4}\right),\qquad(16)$$

where Δk_z^0 is the on-axis phase mismatch ($\boldsymbol{q}_s=\boldsymbol{q}_i=0$). If we use compact detection modes, the projected two-photon field in Eq. (16) will closely resemble the generated field. It should be stressed, however, that both fields contain contribution from all points inside the crystal. The main result in this section, in the form of Eq. (16), is mathematically equivalent to Eq. (10), despite their differing functional forms. One can use either one to calculate the theoretical fine structure; the answers should be the same. The explicit equivalence between the two approaches is presented in Appendix B.

III. EXPERIMENT

A. Experimental setup

The experimental setup used for our experiments is depicted in Fig. 1. We aim at obtaining high resolution images of the near-field correlations present in the two-photon field. This is realized experimentally by using two tightly focused detection modes that can be laterally displaced with respect to each other and by mounting the crystal on a translation stage that permits adjusting its longitudinal position. In the inset of Fig. 1 we illustrate how the back-propagated Gaussian detection modes look like if focused in a certain plane inside the crystal. The waist width $w_d=7$ μm was chosen to provide an optimal tradeoff between the desired resolution and detection efficiency.

The idea behind this setup is similar to the strategy used in confocal microscopy or two-photon microscopy, namely, to eliminate most of the out-of-focus light in order to achieve high lateral and longitudinal resolution. The major difference is that the incoherent nature of the confocal imaging assures that mostly one plane is visualized. In our case both the generation and detection process are coherent, which means that there is a precise phase relationship between light emitted from all different planes. This leads to interesting fourth-order interference effects, to be described below.

Spatially entangled photon pairs are generated by pumping a 5.06-mm-thick periodically polled $KTiOPO_4$ crystal (PPKTP) with a 180 mW krypton-ion laser beam operating at 413.1 nm. The crystal is positioned close to the focus of a $f=50$ mm lens and is mounted on a translation stage. The laser beam is blocked by a coated GaP wafer, while the down-converted photons are transmitted and then separated by a beam splitter. The detection stages comprise objective lenses and computer-controlled actuators that permit positioning and scanning the detectors in the transverse plane. Single counts are registered by two single photon counting modules; coincidence counts are obtained from a fast AND gate with a time window of 1.4 ns. Narrow band interference filters (spectral width 5 nm at 826 nm) placed in front of the detectors assure "quasimonochromatic" operation.

The effect of the on-axis phase mismatch φ is investigated by setting the temperature of the crystal. Based on the temperature dependence of the refractive indexes at the pump and SPDC wavelengths, the derivative $d\varphi/dT\approx1.04$ K^{-1} was calculated and checked experimentally [27].

The imaging system is set up as follows. The focusing lens of $f=50$ mm produces a $M=13\times$ magnification of the SPDC generated light onto an intermediate image plane. The two objective lenses ($f=11$ mm) then image desired regions of the intermediate image plane onto the input tips of two optical fibers with a demagnification factor of $1/28\times$. In order to adjust the proper width of the detection modes we back propagate a diode laser, operating at the same wavelength of the down-converted modes, through the same single-mode optical fibers used for detection. Adjusting the position of the objective lenses we minimize the detection modes width at the image plane to $(w_d)_{image}=85$ μm, as checked with a beam profiler CCD camera. This corresponds to $w_d\approx7$ μm inside the crystal.

The spatial reconstruction of the fourth-order correlation function $V_{\text{proj}}(\boldsymbol{\rho}_-;z)$ is obtained by combining a longitudinal translation of the crystal with transverse scans of the detection stages. By moving the nonlinear crystal toward or away from the lens we can image different slices in the vicinity of the crystal. For each imaged plane we measure the transverse dependence of the coincidence count rate by fixing one detector mode centered at $\boldsymbol{\rho}=\mathbf{0}$ and scanning the other one in the horizontal direction. Since the near-field correlations depend only on the difference coordinate $|\boldsymbol{\rho}_s-\boldsymbol{\rho}_i|$, we are effectively reconstructing $V_{\text{proj}}(\boldsymbol{\rho}_-;z)$. Two remarks are important: due to the magnification factor, moving one detector stage by $M\boldsymbol{\rho}$ causes the detection mode inside the crystal to move by $\boldsymbol{\rho}$, as sketched in Fig. 1. Furthermore, refractive effects stretch the Gaussian detection mode longitudinally; therefore, in order to move the focus from the front facet to the back facet, the crystal needs to be displaced only by a distant L/n. All the presented experimental data are scaled to account for both magnification and refractive effects, i.e., the transverse displacement of the detector stage has been divided by $M=13\times$ and the longitudinal displacement of the crystal has been multiplied by n ($n=1.843$ for PPKTP at 826.2 nm and $T\approx60$ °C). All count rates are corrected for accidental counts.

B. Results and discussion

Our goal is to verify experimentally the main features present in the near-field correlations of the two-photon field,

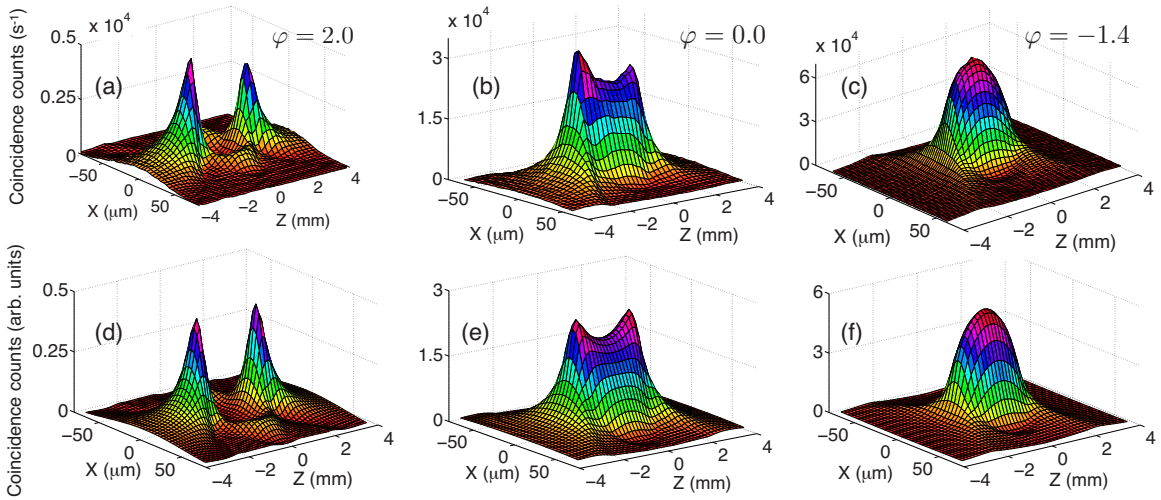

FIG. 2. (Color online) Full spatial dependence of the near-field correlations for different phase mismatches. Figures (a), (b), and (c) show the experimental results for $\varphi=2.0$, $\varphi=0.0$, and $\varphi=-1.4$, respectively. Figures (d), (e), and (f) show the theoretical results, calculated using either Eq. (16) or Eq. (A3). The relative strength (=vertical scale) between the three experimental and the three theoretical plots is determined by a single scaling parameter.

including the full spatial dependence in both transverse and longitudinal coordinates as well as the behavior under phase mismatch. We can calculate the theoretical predictions either from Eq. (16) or Eq. (A3) presented in the Appendix A.

Figure 2 gives an overview of three complete characterizations. The experimental results for $\varphi=2.0$, $\varphi=0.0$, and $\varphi=-1.4$ are displayed in Figs. 2(a)–2(c), respectively. Figures 2(d)–2(f) show the corresponding theoretical predictions. Note that the theoretical curves do not contain any fit parameters, being based only on well-known parameters, such as L, k_0, w_d, and φ. The qualitative agreement between theory and experiments is evident. The theoretical coincidence counts are displayed in arbitrary units, since the theory only provides a proportionality; the fact that the proportionality factor is $\approx 10^4$ is just a coincidence. The relative scaling between plots taken at different temperatures is well defined and agrees with the experimental data.

The obtained three-dimensional results are intriguing. For $\varphi=2.0$ we observe the presence of two very sharp peaks with a low "crater" in between. The distance between the two peaks in the experimental data is 5.3 ± 0.1 mm, while theory predicts a value equal to $L=5.06$ mm. Even for perfect phase-matching ($\varphi=0$), we observe considerably higher counts when the detection modes are focused at either of the crystal facets. The observation of this "surface effect" is limited to observations with compact detection modes ($w_d \approx 7$ μm in our setup). For a detection mode width of $w_d=10$ μm the peaks should be hardly visible, being absent for $w_d=12$ μm (and $\varphi=0$). The effect of the increased detection mode width is to smooth the detected fine structure $V_{\mathrm{proj}}(\boldsymbol{\rho}_-;z)$.

We can interpret these results as follows. Suppose we had a nonmagnified imaging scheme ($M=1$). The plane $z=2.5$ mm corresponds to an image of the output facet of the crystal and can indeed be interpreted as a "copy" of the field in that position. Although the measured correlations in the other planes ($z<2.5$ mm) exist in the vicinity of the image plane, they can no longer be interpreted as an image of the field correlations inside the crystal. The reason is that if one tries to image regions inside the source, light emitted between these regions and the output facet will also contribute, albeit in a "defocused" way. With our measurement we can only describe how the correlations behave in the accessible region around the image plane.

All the peculiar structures shown in Fig. 2 are only present in the fourth-order correlation (=coincidences counts) as no interference effect is observed in the single counts. We confirm this statement by plotting in Fig. 3 the single counts measured by the scanning detector for $\varphi=0$ (perfect phase matching). The single counts behave in the same way for all φ values considered in this work. In the remaining Figs. 4–9 we will discuss in details some specific features of the near-field correlations.

Figure 4 shows how the coincidence rate $|V_{\mathrm{proj}}(\mathbf{0};0)|^2$, recorded on axis ($\boldsymbol{\rho}_-=\mathbf{0}$) and at $z=0$, varies with phase matching. This figure thus shows the relative scaling between the scans performed at different phase mismatches. Note that Fig. 4 is not symmetric with respect to $\varphi=0$ and

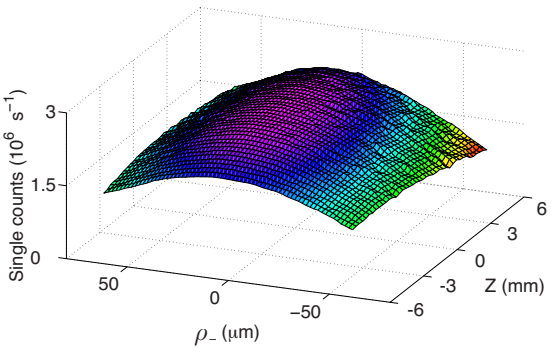

FIG. 3. (Color online) Single counts recorded by the scanning detector while obtaining the correlations in Fig. 2(b). The intensity varies less than 10% in the central region of the scan ($\rho_-<25$ μm). The small residual variations are due to the finite width of the pump beam.

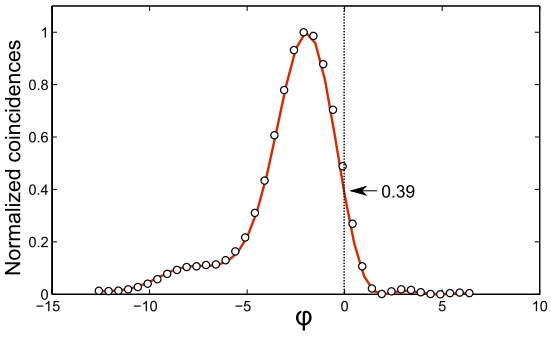

FIG. 4. (Color online) Dependence of the coincidence count rate on the phase mismatch φ. When both detection modes are centered ($\boldsymbol{\rho}_s=\boldsymbol{\rho}_i=\mathbf{0}$) and focused at the center of the crystal ($z=0$). The phase mismatch can be adjusted by changing the temperature of the crystal. The open circles are experimental; the continuous (red) curve the theoretical result. No curve fitting was performed. The asymmetry of the curve depends sensitively on the width of the detection mode (see text). For our experimental realization, the coincidence count rate at $\varphi=0.0$ is only 39% of its maximum value, which is achieved at $\varphi=-2.0$.

peaks at $\varphi=-2.0$ rather than at $\varphi=0.0$. Equation (16) predicts that the asymmetry of the curve is basically determined by the size of the detection modes. In the limit $w_d\to 0$ (or $z_n\to 0$) the theoretical curve is highly asymmetric, while the curve becomes approximately symmetric under $\varphi\leftrightarrow-\varphi$ for large w_d, when the Rayleigh range $z_n=\frac{1}{2}kw_d^2$ of the detection modes becomes much larger than the crystal thickness. This can be understood physically by noticing that for a very large detection width all the down-converted light is collected; one then effectively measures the overall SPDC efficiency as a function of the phase mismatch, recovering the standard "sinc" curve.

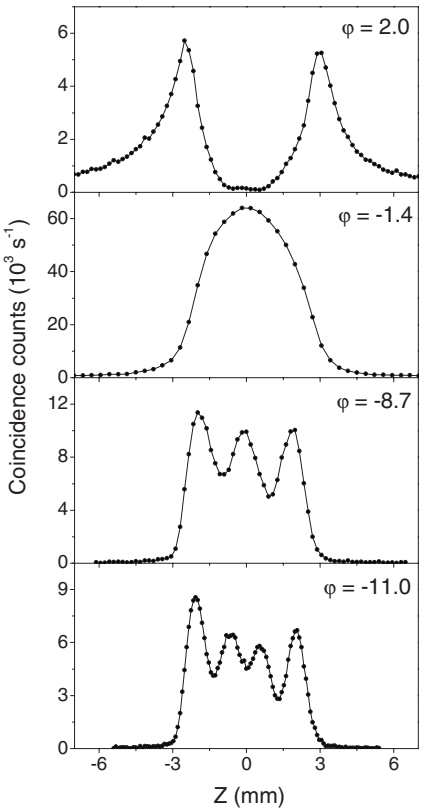

FIG. 5. Axial correlations ($\boldsymbol{\rho}_s=\boldsymbol{\rho}_i=\mathbf{0}$) in the near field for different phase mismatches φ. This figure demonstrates the intriguing dependence of the measured on-axis correlations on the focusing plane z.

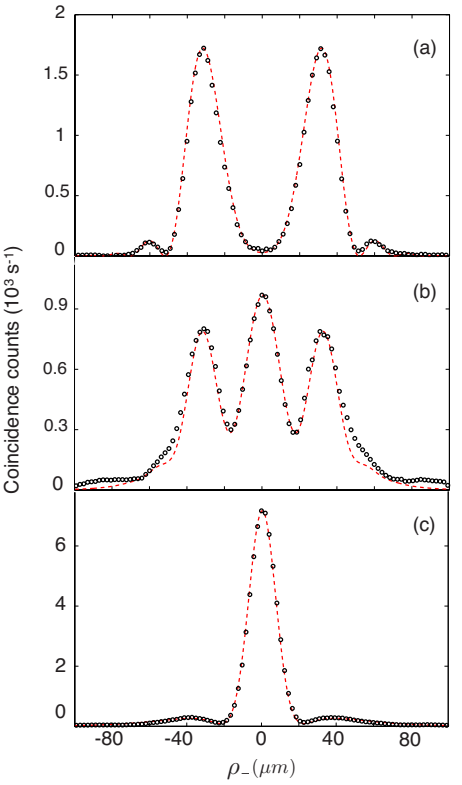

FIG. 6. (Color online) Transverse correlations for $\varphi=2.0$ in three different z planes. These plots correspond to transverse cuts of Fig. 2(a) taken at the planes (a) $z_a=0$, (b) $z_b=0.3L/2$, and (c) $z_c=L/2$. The open circles are experimental data; the dashed (red) curves are the theoretical predictions. Fig. (a) exhibits spatial antibunching (see text).

Figure 5 shows the dependence of the on-axis $\boldsymbol{\rho}_-=\mathbf{0}$ coincidence rate on the longitudinal position z of the detection

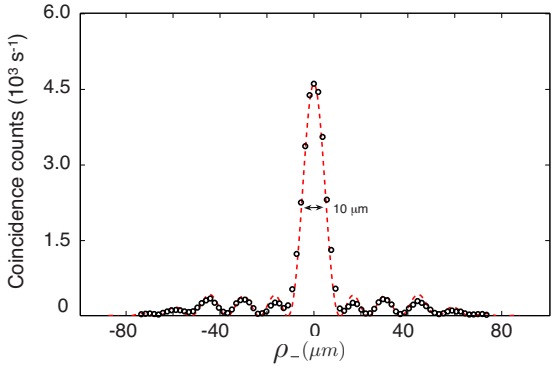

FIG. 7. (Color online) Transverse correlations for $\varphi=-8.2$ and $z=0$. This curve demonstrates that it is possible to achieve very narrow central peaks by adjusting the phase mismatch φ; the central peak has a FWHM of only 10 μm.

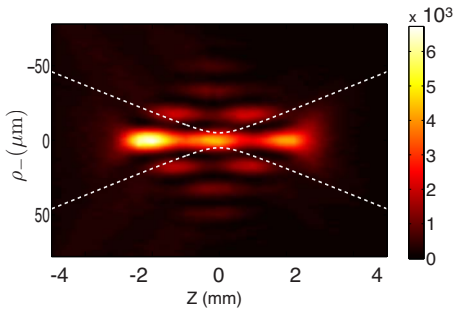

FIG. 8. (Color online) Density plot of the fourth-order correlation for a full spatial scan performed at $\varphi=-8.2$. The curve shown in Fig. 7 retains its width over a relatively long z range, much longer than if it were a Gaussian beam. The white dashed curve shows how a Gaussian beam with the same waist (FWHM=10 μm) would diffract; at $\lambda=826.2$ nm the Rayleigh range of this beam is $z_0=274$ μm. The persistence of the narrow structure in the measured coincidence rate is maintained by interference with light from the many side peaks; a similar phenomenon occurs in a Bessel beam.

foci. The experimental z scans of $|V_{\text{proj}}(\mathbf{0};z)|^2$ are measured for $\varphi=2.0$, $\varphi=-1.4$, $\varphi=-8.7$, and $\varphi=-11.0$. All results are in accord with our expectations (not shown) apart from a small asymmetry in the signal observed when the detected foci are positioned either at the facet closest to the lens ($z=-L/2$) or at the far facet ($z=+L/2$). We attribute the observed asymmetry to spherical aberration in the focused detection modes,

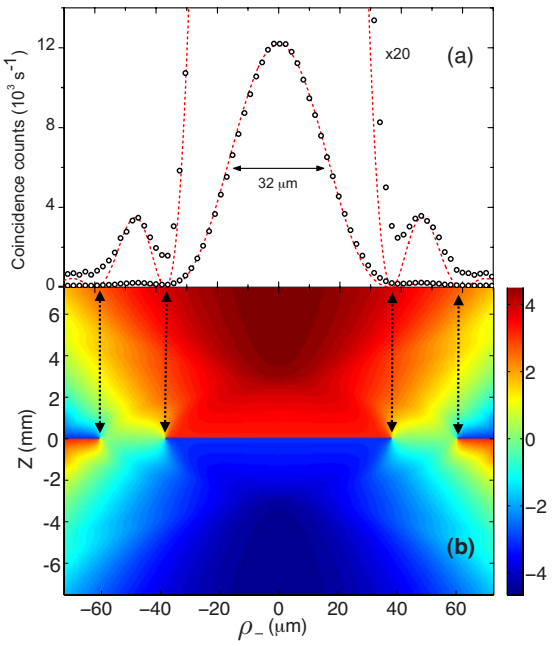

FIG. 9. (Color online) (a) Transverse correlations at perfect phase-matching ($\varphi=0.0$) and $z=0$. The open circles are experimental data; the dashed (red) line is a theoretical prediction. The FWHM of both experimental and theoretical curves is 32 μm. In the 20× magnified plot small side peaks are visible. (b) False-color plot of the theoretical phase surfaces obtained from the complex valued amplitude $V_{\text{proj}}(\boldsymbol{\rho}_-;z)$. The arrows indicate the presence of fourth-order phase singularities at the points where the correlation function is zero valued.

induced by their transition through the air-crystal interface; this aberration would make the waist of the detector modes somewhat larger when it is positioned at the far facet as compared to the near facet of the generating crystal.

Figure 5 shows that the phase mismatch has a dramatic effect on the axial correlations. The range within which the coincidence counts are appreciable is bounded by the crystal thickness $L=5.06$ mm, but its precise shape follows from Eq. (16), which for $\boldsymbol{\rho}_-=\mathbf{0}$ translates into

$$|V_{\text{proj}}(\mathbf{0};z)|^2 \propto \left| \int_{-L/2-z}^{+L/2-z} dz' \frac{\exp(-i\Delta k_z z')}{(z'-iz_n)} \right|^2. \quad (17)$$

Equation (17) is identical to a classical formula [32] for the intensity of second harmonic generation (SHG) in a medium pumped by a tightly focused Gaussian beam. The shapes presented in Fig. 5 are indeed similar to those obtained in the context of SHG [32,33]. We have thus shown that the strong dependence of the longitudinal (z) correlations with phase mismatch is also present in the two-photon correlation measurements in SPDC. Theoretical studies for axial correlations have been performed before by Nasr *et al.* [25]. They also concluded that strong axial correlations are only found in a region around the image plane bounded by the thickness of the crystal L (divided by the refractive index). However, their exact predictions differs from ours due to an assumption that the system could be treated in only one dimension. This point is further discussed in Appendix A, where we also obtain an analytical expression for the axial correlations at perfect phase matching.

Figure 6 shows the transverse correlations at $\varphi=-2.0$ as measured and calculated for three different z planes: (a) $z_a=0$, (b) $z_b=0.3L/2$, and (c) $z_c=L/2$. That is, the detection modes are focused at the center of the crystal, at an intermediate plane, and at the facet, respectively. These curves are examples of how we can find a rich set of non-bell-shaped transverse correlations in the near field that are not yet discussed in the literature. Notice how the transverse profile of the coincidence rate changes with the focusing plane. If one focus the detection modes at either crystal surface there is a maximum probability of finding the two photons "together" at $\boldsymbol{\rho}=\mathbf{0}$. If the detection modes are focused in the center ($z=0$), this probability drops to practically zero, i.e., the two photons are spatially antibunched [34,35]. This observation of antibunching is sufficient to reveal the quantum nature of the correlations (as long as the field is also homogeneous, which is the case). We have discussed this aspect in [16].

We can also interpret Fig. 6 imagining, once again, a scheme with unit magnification. There is a plane before $z<0$ where the photon pairs are found predominantly together in the same transverse position. In the plane $z=0$ this situation is reversed, and the photons are antibunched, i.e., there is a zero probably of finding them at the same position. The symmetry $z\leftrightarrow -z$ assures that for $z>0$ the photons will be once again bunched. The transition of an axial valley to an axial peak in near-field imaging also appears in the context of Fresnel diffraction. It is solely due to free space propagation of the field. The two-photon field propagate in a similar

fashion, but instead of a zero in intensity there is a zero in coincidences counts.

Figure 7 shows how the central peak for transverse correlations can get very narrow in certain configurations. We show the results obtained for a transverse scan at $z=0$ and $\varphi=-8.2$. The full width at half maximum (FWHM) of this peak is only 10 μm as indicated. Quite surprisingly, this narrow width can maintain itself without being diffracted over a z range as long as the crystal thickness L. To stress this point we show in Fig. 8 a false color plot of the measured fourth-order correlation over the full z range. The white dashed curves indicate how a Gaussian beam with the same FWHM at its waist would diffract; the Rayleigh range of this beam is $z_0=274$ μm at $\lambda=826.2$ nm. We can see that the fourth-order correlation pattern retains its narrow width for much longer than the corresponding Gaussian beam. These correlations are also less "diffractive" as compared to a Gaussian beam with the de Broglie wavelength of the biphoton $\lambda/2=413.1$ nm. This behavior is a consequence of the many side peaks that can be clearly identified. In this respect, it resembles the propagation characteristics of Bessel-like beams.

Recently, the possibility of achieving extreme biphoton spatial localization in the near field by resolving the photon pairs temporally, and vice versa, was theoretically proposed [36]. Figure 7 experimentally proves that high spatial localization can also be achieved by controlling the phase-matching conditions. For thinner crystals and smaller values of φ, peaks as narrow as 4 μm can be produced.

Next we compare the narrow-ranged correlations discussed above with those obtained at the most common experimental setting $\varphi=0$ (perfect phase matching). Figure 9(a) shows the experimental and theoretical results for a transverse scan at $z=0$. A 20× magnified plot is also shown in order to highlight the superiority of the correct theoretical expression over Gaussian approximations. The FWHM of this curve is 32 μm, thus being about 3× larger than the curve taken at $\varphi=-8.2$. and presented in Fig. 7.

Our theoretical formulation also provides the phase structure of the "wave function" in the near field. Figure 9(b) shows a density plot of the theoretical phase surfaces obtained directly from the complex-valued amplitude $V_{\mathrm{proj}}(\boldsymbol{\rho}_-;z)$. The phase is unwrapped in such a way that all phase jumps are related to phase singularities. These phase singularities are associated with the points where we expect a zero for the two-photon correlation. These singularities are thus not of the standard type, related to zeros of field intensities, but are related to zeros of the fourth-order correlation function. It has been shown recently that an optical vortex can be transferred from the pump beam to the biphoton correlation [37]. Here we argue that those "fourth-order phase singularities" also arise due to phase matching.

A word of caution. Some authors consider the near-field imaging as an imaging of the *birthplace* of the photon pairs [8]. As we have seen, this statement is not very accurate. The physical origin of the observed correlations is always interference of photon pairs generated at all possible sites in the crystal. There is a coherent superposition of localized emissions from all these sites. The combined effect of all production events, propagated to the observation plane, leads to the measured fourth-order interference patterns. The collinear phase mismatch φ is a crucial component in the description since it changes the relative phase of photon pairs generated at different "slices" in the crystal. This strongly modifies the propagation and, therefore, the resulting interference. The presence in Fig. 2 of either photon bunching or antibunching, which is not in contradiction with the assumption of (a superposition of) localized emissions, illustrates very well the point.

Finally we would like to discuss the implications of our results to measurements of the dimensionality of the spatial entanglement. Recently Howell *et al.* proposed and implemented a realization of the Einstein-Podolsky-Rosen (EPR) paradox, i.e., the violation of a separability criterion in the position-momentum domain, using entangled photon pairs [8]. One of their key measurements is similar to the one presented in Fig. 9(a). At that time the existence of a richer structure in the near field was not yet known. We can now revisit their experiment and pose new questions. To obtain the same results the authors could have chosen to image either the back or front facet of the crystal, but not the center. Strangely enough, we find that the violation of the separability criterion depends on which plane is being imaged. The reason is that this criterion depends only on field intensities, while entanglement may also exist in the phase structure, which, as we illustrated, is not trivial. We provide in this way experimental support to proposed entanglement migration between amplitude and phase [38]. Additionally, the existence of more complex non-bell-shaped transverse profiles at $\varphi\neq 0$, like the ones presented in Fig. 6, indicates that a larger number of modes is necessary to perform a Schmidt decomposition [10] and, consequently, a higher degree of spatial entanglement for nonperfect phase matching is to be expected. We have recently observed this phenomenon [39].

IV. CONCLUSION

In this work we have explored the near-field correlations in the two-photon field generated by spontaneous parametric down conversion. Two different theoretical approaches were presented, each one leading to a different integral representation of the field. Numerical simulations can be performed using either formula, both providing the same predictions. In order to experimentally access the correlations in the near field a new regime of operation was introduced, in which the width of the detection modes is determined by an optimal trade off between resolution and detection efficiency. The detection modes should be small enough to obtain sufficient spatial resolution, but large enough not to loose too many coincidence counts.

The phase-matching condition, imposed by the finite thickness of the crystal, leads to some remarkable features. Among them we highlighted the observation of intriguing three-dimensional structures, the presence of spatial antibunching, a link with previous results in second harmonic generation, the observation of correlations that resemble Bessel beams in propagation, and the prediction of fourth-order phase singularities. Furthermore, the operation under phase mismatch reveals a rich set of non-bell-shaped spatial

correlations. We have already obtained evidence that this higher complexity leads to a higher degree of spatial entanglement [39].

ACKNOWLEDGMENTS

The authors acknowledge fruitful discussions with C. H. Monken and J. P. Woerdman. This work has been supported by the "Stichting voor Fundamenteel Onderzoek der Materie (FOM)" and by the EU under the FET-Open Agreement "HIDEAS," Grant No. FP7-ICT-221906.

APPENDIX A

In this appendix we will present an analytical result for the on-axis correlation $V(\boldsymbol{\rho}_-=0;z)$ for perfect phase-matching ($\varphi=0$). Our starting point is Eq. (10). We substitute Eq. (9) for $V(\boldsymbol{\rho}_-;z)$ and consider Gaussian shaped detection modes

$$\phi_j(\boldsymbol{\rho}_j-\boldsymbol{\rho}_j')\propto\exp\left[-\frac{(\boldsymbol{\rho}_j-\boldsymbol{\rho}_j')^2}{w_d^2}\right], \tag{A1}$$

where w_d is the width of the detection mode in the focused z plane. After integrating over the transverse coordinates $\boldsymbol{\rho}_s'$ and $\boldsymbol{\rho}_i'$ we obtain

$$V_{\mathrm{proj}}(\boldsymbol{\rho}_-;z)\propto\int_{-\infty}^{+\infty}d\boldsymbol{q}\ \ \mathrm{sinc}\left(\frac{L|\boldsymbol{q}|^2}{2nk_0}+\varphi\right)\times\exp\left[-\frac{|\boldsymbol{q}|^2w_d^2}{2}-i\frac{|\boldsymbol{q}|^2}{k_0}z-i\boldsymbol{q}\cdot\boldsymbol{\rho}_-\right]. \tag{A2}$$

This equation is rotationally symmetric and can be integrated over the azimuthal angle to yield

$$V_{\mathrm{proj}}(\rho_-;z)\propto\int_0^{+\infty}dy\ \ \mathrm{sinc}\left(\frac{L}{2nk_0}y+\varphi\right)\mathrm{J}_0(\sqrt{y}\rho_-)\times\exp\left[-\left(\frac{w_d^2}{2}+i\frac{z}{k_0}\right)y\right], \tag{A3}$$

where $\rho_-\equiv|\boldsymbol{\rho}_-|$, $y=|\boldsymbol{q}|^2$, and J_0 is the 0th order Bessel function. Most of our numerical simulations were performed using this equation.

Next we consider the axial correlations ($\rho_-=0$) for perfect phase matching ($\varphi=0$). In this case, Eq. (A3) has an analytical solution, the square of which is the coincidence counting rate

$$R_{cc}(0;z)\propto|V_{\mathrm{proj}}(0;z)|^2\propto\left|\arctan\left[\frac{L}{n}\frac{1}{k_0w_d^2+2iz}\right]\right|^2. \tag{A4}$$

Equation (A4) shows how the ratio $R_{cc}(0;L/2n)/R_{cc}(0;0)$ between the coincidence rates observed with both detection foci positioned either at the facets or in the center depends sensitively on the size of the detection modes. For our experiments this width is $w_d=7$ μm, which leads to a ratio $R_{cc}(0;L/2n)/R_{cc}(0;0)=1.25$, both theoretically and experimentally. For smaller w_d this ratio is expected to increase, leading to a divergence for $w_d\to0$.

This result differs from the theoretical predictions presented in [25]. The reason is that the authors of Ref. [25] assume that the system can be treated one-dimensionally without loss of generality. The integrated sinc function present in Eq. (A2), however, behaves quite differently if its argument is a one-dimensional or bidimensional vector. Equation (A4) is the correct expression for a realistic three-dimensional system.

APPENDIX B

In this appendix we will show explicitly the equivalence between the key Eq. (10), similar to Eqs. (A2) and (16). We start with Eq. (A2) and write the "sinc" function as

$$\mathrm{sinc}\left(\frac{L|\boldsymbol{q}|^2}{2nk_0}+\frac{L}{2}\Delta k_z^0\right)=\frac{1}{L}\int_{-L/2}^{+L/2}\exp\left(\frac{i|\boldsymbol{q}|^2}{nk_0}z''+i\Delta k_z^0z''\right)\mathrm{d}z'', \tag{B1}$$

where we used the definition of the collinear phase mismatch $\varphi=\frac{L}{2}\Delta k_z^0$. Next we make a change of variables $z'=nz-z''$. We now recognize the original integral in $\boldsymbol{q}$ as the Fourier transform of a complex Gaussian function. It can be immediately evaluated

$$\int_{-\infty}^{+\infty}(\cdots)\mathrm{d}\boldsymbol{q}=\exp\left(\frac{i}{4}\frac{k\rho_-^2}{z'-iz_n}\right)\frac{i\pi k}{z'-iz_n}, \tag{B2}$$

where $z_n=\frac{1}{2}nk_0w_d^2$. We can thus recover Eq. (16), which reads

$$V(\rho_-;z)\propto\int_{-L/2-nz}^{+L/2-nz}\mathrm{d}z'\frac{\exp(-i\Delta k_z^0z')}{z'-iz_n}\exp\left(\frac{i}{4}\frac{k\rho_-^2}{z'-iz_n}\right). \tag{B3}$$

[1] R. H. Brown and R. Twiss, Nature (London) **177**, 27 (1956).
[2] C. K. Hong and L. Mandel, Phys. Rev. A **31**, 2409 (1985).
[3] B. R. Mollow, Phys. Rev. A **8**, 2684 (1973).
[4] Y. H. Shih and C. O. Alley, Phys. Rev. Lett. **61**, 2921 (1988).
[5] T. Yarnall, A. F. Abouraddy, B. E. A. Saleh, and M. C. Teich, Phys. Rev. Lett. **99**, 170408 (2007).
[6] D. Bouwmeester, J.-W. Pan, K. Mattle, M. Eibl, H. Weinfurter, and A. Zeilinger, Nature (London) **390**, 575 (1997).
[7] A. V. Sergienko, M. Atatüre, Z. Walton, G. Jaeger, B. E. A. Saleh, and M. C. Teich, Phys. Rev. A **60**, R2622 (1999).
[8] J. C. Howell, R. S. Bennink, S. J. Bentley, and R. W. Boyd, Phys. Rev. Lett. **92**, 210403 (2004).
[9] M. V. Fedorov, M. A. Efremov, P. A. Volkov, E. V. Moreva, S. S. Straupe, and S. P. Kulik, Phys. Rev. A **77**, 032336 (2008).

[10] C. K. Law and J. H. Eberly, Phys. Rev. Lett. **92**, 127903 (2004).
[11] S. P. Walborn and C. H. Monken, Phys. Rev. A **76**, 062305 (2007).
[12] C. H. Monken, P. H. Souto Ribeiro, and S. Pádua, Phys. Rev. A **57**, 3123 (1998).
[13] B. E. A. Saleh, A. F. Abouraddy, A. V. Sergienko, and M. C. Teich, Phys. Rev. A **62**, 043816 (2000).
[14] A. V. Burlakov, M. V. Chekhova, D. N. Klyshko, S. P. Kulik, A. N. Penin, Y. H. Shih, and D. V. Strekalov, Phys. Rev. A **56**, 3214 (1997).
[15] M. Tsang, Phys. Rev. A **75**, 043813 (2007).
[16] H. Di Lorenzo Pires and M. P. van Exter, Phys. Rev. A **79**, 041801(R) (2009).
[17] P. H. Souto Ribeiro, C. H. Monken, and G. A. Barbosa, Appl. Opt. **33**, 352 (1994).
[18] I. F. Santos, J. G. Aguirre-Gómez, and S. Pádua, Phys. Rev. A **77**, 043832 (2008).
[19] A. Valencia, G. Scarcelli, M. D'Angelo, and Y. Shih, Phys. Rev. Lett. **94**, 063601 (2005).
[20] H. M. Ozaktas and D. Mendlovic, J. Opt. Soc. Am. A Opt. Image Sci. Vis **12**, 743 (1995).
[21] P. Pellat-Finet, Opt. Lett. **19**, 1388 (1994).
[22] P. Pellat-Finet and G. Bonnet, Opt. Commun. **111**, 141 (1994).
[23] D. S. Tasca, S. P. Walborn, P. H. Souto Ribeiro, and F. Toscano, Phys. Rev. A **78**, 010304(R) (2008).
[24] A. F. Abouraddy, B. E. A. Saleh, A. V. Sergienko, and M. C. Teich, J. Opt. Soc. Am. B **19**, 1174 (2002).
[25] M. B. Nasr, A. F. Abouraddy, M. C. Booth, B. E. A. Saleh, A. V. Sergienko, M. C. Teich, M. Kempe, and R. Wolleschensky, Phys. Rev. A **65**, 023816 (2002).
[26] M. D'Angelo, A. Valencia, M. H. Rubin, and Y. Shih, Phys. Rev. A **72**, 013810 (2005).
[27] W. H. Peeters and M. P. van Exter, Opt. Express **16**, 7344 (2008).
[28] O. Cosme, A. Delgado, G. Lima, C. H. Monken, and S. Pádua, e-print arXiv:0906.4734.
[29] M. H. Rubin, Phys. Rev. A **54**, 5349 (1996).
[30] W. H. Peeters, J. J. Renema, and M. P. van Exter, Phys. Rev. A **79**, 043817 (2009).
[31] B. E. A. Saleh, M. C. Teich, and A. V. Sergienko, Phys. Rev. Lett. **94**, 223601 (2005).
[32] D. A. Kleinman and R. C. Miller, Phys. Rev. **148**, 302 (1966).
[33] D. A. Kleinman, A. Ashkin, and G. D. Boyd, Phys. Rev. **145**, 338 (1966).
[34] W. A. T. Nogueira, S. P. Walborn, S. Pádua, and C. H. Monken, Phys. Rev. Lett. **86**, 4009 (2001).
[35] D. P. Caetano and P. H. Souto Ribeiro, Phys. Rev. A **68**, 043806 (2003).
[36] A. Gatti, E. Brambilla, L. Caspani, O. Jedrkiewicz, and L. A. Lugiato, Phys. Rev. Lett. **102**, 223601 (2009).
[37] R. M. Gomes, A. Salles, F. Toscano, P. H. Souto Ribeiro, and S. P. Walborn, Phys. Rev. Lett. **103**, 033602 (2009).
[38] K. W. Chan, J. P. Torres, and J. H. Eberly, Phys. Rev. A **75**, 050101(R) (2007).
[39] H. Di Lorenzo Pires, C. H. Monken, and M. P. van Exter, Phys. Rev. A **80**, 022307 (2009).